JOURNAL OF PROPULSION AND POWER
Vol. 20, No. 2, March–April 2004

Sonic Injection into a Mach 5.0 Freestream Through Diamond Orifices

Rodney D. W. Bowersox*
Texas A&M University, College Station, Texas 77843
and
Huaiguo Fan† and Daina Lee†
University of Alabama, Tuscaloosa, Alabama 35487

An experimental study to characterize the near-field ($x/d < 8.0$) flow for sonic air injection through 15-deg half-angle diamond-shaped orifices at four incidence angles (10, 27.5, 45, and 90 deg) and two total pressures (0.10 and 0.46 MPa) into a high Reynolds number (53×10^6) Mach 5.0 freestream was performed. A 90-deg circular injector, with the same exit port area and total pressures, was examined for comparative purposes. The experimental methods included surface oil flow visualization, shadowgraph photography, Mie scattering flow visualization, pressure-sensitive paint, and a pitot–cone five-hole pressure probe. Flowfield documentation, jet penetration, and shock-induced total pressure loss were derived from these data. Attachment of the interaction shock wave was found to depend on both incidence angle and injector pressure. Penetration correlations were developed for both the diamond and circular injectors. An approximate analysis indicated that the shock-induced total pressure loss decreased with decreasing incidence angle and injection pressure, and the largest losses were incurred by the 90-deg circular injector.

Nomenclature

C_D	=	discharge coefficient
d	=	effective geometric diameter, 4.89 mm
d_H	=	hydraulic diameter
I	=	image intensity
J	=	$\rho_j u_j^2 / \rho_\infty u_\infty^2$
J_{eff}	=	$J \cdot \sin(\alpha)$
M	=	Mach number
p	=	pressure
R	=	$\rho_j u_j / \rho_\infty u_\infty$
T	=	temperature
x	=	axial coordinate
y	=	transverse coordinate
y_p	=	penetration
z	=	lateral coordinate
α	=	incidence angle relative to x axis, positive counterclockwise
Δ	=	shock standoff distance
δ	=	boundary-layer thickness
δ^*	=	boundary-layer displacement thickness
λ	=	p_{eb} / p_∞
ξ	=	$J_{\text{eff}}^m (x/d)^n$
Π	=	average stagnation pressure ratio
ρ	=	dsensity

Subscripts

c	=	cone surface
eb	=	effective back
j	=	injector
max	=	maximum shock location
n	=	normal
ref	=	reference pressure, 1.0 atm
t	=	stagnation condition
2	=	downstream of a shock wave
∞	=	freestream

Received 3 December 2002; revision received 26 August 2003; accepted for publication 26 August 2003.

*Associate Professor, Aerospace Engineering. Associate Fellow AIAA.
†Graduate Research Assistant, Aerospace Engineering and Mechanics.

Introduction

THE supersonic combustion ramjet (scramjet) is a leading engine candidate for sustained hypersonic flight within the atmosphere.[1–3] Efficient and rapid fuel–air mixing within the scramjet is an important long-standing technological challenge.[3,4] The primary difficulty is the short fuel–air residence time within the engine. Compounding this challenge is that compressibility slows shear layer mixing. Furthermore, at high Mach numbers, the thrust margins are relatively small. Hence, minimizing total pressure loss, that is, drag, is also an important factor in developing a suitable fuel injection scheme that often competes with achieving rapid mixing rates.

Scramjet fuel injection has received considerable attention since the mid-1950s[3] and numerous fuel injector concepts have been studied.[3,5,6] In summary, two basic injector categories have emerged, flush wall and physical ramp. A combination of both types has also been studied.[7] The present study is relevant to flush–swall injection.

The flow structure of perpendicular injection of an underexpanded jet, which is the prevalent operating condition for scramjet applications, into a supersonic freestream has been thoroughly documented.[8–11] In summary, the first flow feature, progressing in the streamwise flow direction, is a bow shock produced as the freestream impacts the injection streamtube.[8] For injector configurations, where δ/d is on the order of one or more, a separation region and a lambda shock form upstream of the injector port.[9] A horseshoe vortex forms between the jet and the interaction shock.[10] After entering the freestream, the underexpanded jets experience a rapid Prandtl–Meyer expansion surrounded by a barrel shock.[8] A shock wave normal to the jetpath, known as the Mach disk, terminates the barrel shock and compresses the flow to the effective backpressure p_{eb}.[9] Downstream of the Mach disk, a counter-rotating vortex pair forms within the jet plume.[11] Wake vortices are also formed.[10] The plume vorticity and turbulent mechanisms induce the required large-scale mixing between the jet fluid and the freestream.

Angled injection is a means of the reducing total pressure loss associated with the strong bow shock. Furthermore, low angled injection has been shown to create a measurable increase in the overall combustion thrust potential,[5,12] as compared to normal injection. For

both angled and normal injection, the penetration has been shown to increase with increasing jet momentum, that is, (Ref. 2).

The influence of port geometry (elliptical, wedge, and diamond) has also been studied.[13–16] Overall, the flowfield for injection through an elliptical port ($M_\infty = 2.0, M_j = 1.0$), with the major axis aligned with the flow, was similar to that of a corresponding circular port.[13] One notable feature for the elliptical port was that the jet flow expanded more in the direction of the minor axis. The primary beneficial flowfield attribute of sharp leading-edge injectors is weaker, in some cases attached, leading-edge jet interaction shocks.[14–16] In terms of performance, weaker shocks produce lower shock-induced total pressure loss, that is, reduced fuel-injector-induced drag for scramjet applications, as compared to the bow shocks generated by conventional circular injectors. In addition, weaker shocks minimize the shock-induced upstream flow separation, which translates into reduced surface heat transfer near the injector. In addition, far-field penetration has been documented to increase with diamond injectors as compared to more conventional circular injection.[16]

The objective for the present study was to experimentally characterize the near-field flow for sonic air injection through 15-deg half-angle diamond-shaped orifices at various incidence angles. The present study was performed at Mach 5.0, which corresponds to vehicle flight Mach numbers near 12–14 (Ref. 3). In summary, an experimental investigation of underexpanded sonic injection through a diamond orifice at four incidence angles (10, 27.5, 45, and 90 deg) and two total pressures ($P_{tj} = 0.10$ and 0.46 MPa) was performed. A 90-deg circular injector at the same two total pressures was also examined for comparative purposes. The experimental methods included surface oil flow visualization, shadowgraph photography, Mie scattering flow visualization, pressure-sensitive paint (PSP), and a pitot–cone five-hole pressure probe. Flowfield documentation, jet penetration, and shock-induced total pressure loss were derived from these data.

Facilities and Instrumentation

Wind-Tunnel and Injector Models

A high Reynolds number, Mach 5 blowdown wind tunnel was used for the present experiments. Shown in Fig. 1 is the coordinate system and test section, and the freestream flow conditions are listed in Table 1. The test section had a 76.2 × 76.2 mm cross-sectional area, with a length of 266.7 mm. The test section sidewalls had optical-grade glass windows (flat to within 52.0 nm/cm) for optical measurements.

Diamond injectors with 15-deg semivertex angles were used. The semivertex angle and injector size were chosen as compromise between the goals of 1) weak or attached leading-edge shock waves, 2) minimization of shock reflections from the tunnel sidewalls, and 3) manufacturability. Four incidence angles, 10, 27.5, 45, and 90 deg, relative to the axial freestream flow direction were tested. A schematic for the injectors is given in Fig. 2. Each injector had a port area of 18.8 mm^2; the equivalent diameter d, based on area, was 4.89 mm. The injectors were mounted on the bottom plate of the test section as shown in Fig. 1, and the leading edge of the diamond injector was located 71.4 mm downstream of the nozzle exit. The circular injector had an exit diameter of 4.89 mm and an incidence angle of 90 deg; a schematic of this injector is included in Fig. 2. The injectant gas was air, and the jet exit Mach number was 1.0. Two jet total pressures, 0.10 (±1.0%) and 0.46 MPa (±3.0%), were tested. The jet total temperature was 295±3.0 K. Hence, the velocity ratio (u_j/u_∞) was 0.41 for all of the test cases.

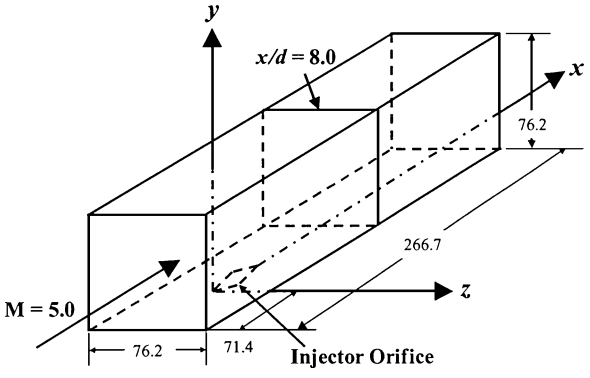

Fig. 1 Test section schematic with coordinate system definition, millimeters.

Table 1 Freestream flow conditions

Parameter	Value
Mach	4.95 ± 2.0%[a]
P_t, MPa	2.40 ± 4.0%[b]
T_t, K	360 ± 3.0%[b]
Re/m ($\times 10^6$)	53
δ, mm	7.6 ± 7.0%[c]

[a]Variation across the freestream.
[b]Held constant to within this amount.
[c]Variation across the tunnel span.

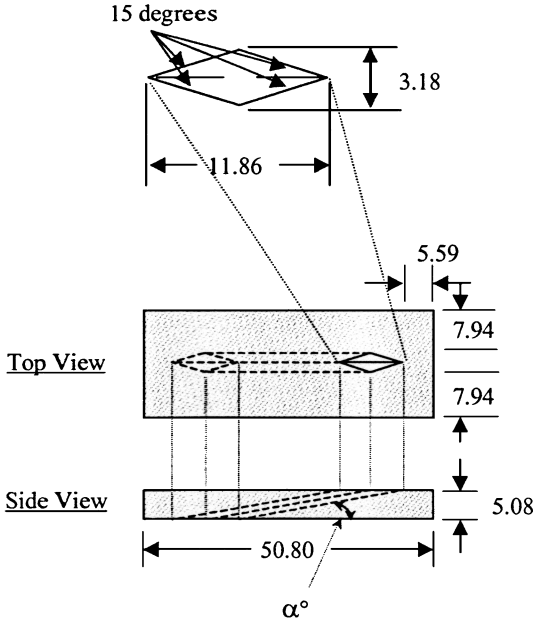

a) Diamond injectors, α = 10–90 deg

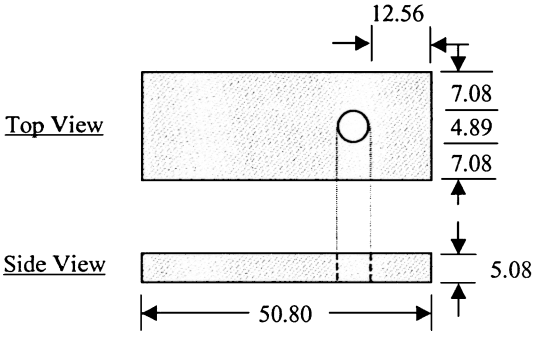

b) 90-deg circular injector

Fig. 2 Injector model schematics, millimeters.

Discharge coefficients for all five injectors at both operating pressures were measured by injecting into a vacuum tank while monitoring the tank pressure and temperature. The entrance region charts of Deissler[17] were used to estimate pressure loss for each injector. The hydraulic diameter[18] d_H for the diamond injectors was 3.0 mm; for the circular injector, it was 4.89 mm. The estimated jet-to-freestream static pressure, mass flux, and momentum ratio are listed in Table 2. The average injector boundary-layer displacement thickness, also listed in Table 2, was estimated as $\delta^*/d = d_H \cdot (1 - C_D^{1/2})/2d$. The

Table 2 Jet flow conditions

α,[a] deg	C_D (±0.03)	p_j/p_∞	R	J	δ^*/d	Δ/d[c]	y_p/d[d]	λ	p_j/p_{eb}	Π
10.0	0.23	8.4	0.20	0.08	0.160	AS	1.9	1.2	7.0	0.99
27.5	0.41	9.7	0.39	0.16	0.110	AS	2.6	1.3	7.5	0.95
45.0	0.67	10.0	0.67	0.27	0.055	0.31	3.0	1.6	6.3	0.89
90.0	0.94	10.3	0.97	0.40	0.009	0.86	3.4	2.0	5.4	0.78
90.0[b]	0.98	10.3	1.03	0.42	0.003	1.30	3.3	2.0	5.4	0.71
10.0	0.24	41.1	1.00	0.41	0.150	AS	2.5	1.4	29.4	0.94
27.5	0.41	45.5	1.87	0.76	0.110	0.24	3.5	1.7	26.8	0.84
45.0	0.68	46.4	3.18	1.29	0.054	0.51	4.1	1.7	27.3	0.74
90.0	0.91	46.7	4.29	1.74	0.014	1.30	4.7	2.0	23.4	0.70
90.0[b]	0.90	47.3	4.27	1.73	0.026	2.90	4.8	2.2	21.5	0.69

[a]First five entries correspond to $P_{tj} = 0.10$ MPa (±1.0%); the second five correspond to $P_{tj} = 0.46$ MPa (±3.0%).
[b]Circular injector.
[c]AS.
[d]Where $x/d = 7.5$.

remaining columns in Table 2 are described in the Results and Discussion section.

Oil Surface Flow Visualization

Dow Corning 200 fluid (dimethicon) with a kinematic viscosity of 1000 cS, which is a medium-viscosity linear polydimethylsiloxane polymer, was used for surface oil-flow visualization. Day-Glo Color T-15 blaze orange fluorescent pigment was mixed with the fluid. The mixture was spread onto the bottom surface of the test section and illuminated by an ultraviolet lamp through an optical grade Plexiglas® ceiling. Photographs of the oil patterns were taken as the tunnel was running with a Kodak Professional DCS 460 color digital camera that was mounted on a tripod the above the tunnel ceiling. The Kodak camera back, which was attached to a Nikon N90 camera body, had a 3060 × 2036 pixel, 12-bit color charge-coupled device (CCD) imager.

Mie Scattering Flow Visualization

Two types of Mie scattering flow visualization images were acquired, instantaneous and time averaged. For the instantaneous images, two pulsed Continuum Surelite Nd:YAG were used. The pulse duration was 10 ns, and the repetition rate was 10 Hz. The lasers produced two coherent green (532-nm) beams. One beam was used to pump a dye [SulfaRhodamine (640-nm) methyl alcohol solution] laser to generate a red (640-nm) beam. The two (green and red) laser beams were merged in space with a dichroic splitter, and the resulting collocated beams were passed through sheet-forming optics and directed into the test section through an optical grade Plexiglas ceiling. The temporal delay between the red and green laser was set at 200 ns with a Stanford Research Systems Model DG535 four-channel digital delay/pulse generator. The two-color system allowed for instantaneous velocity measurement.[15] A TSI Model 9306 six-jet atomizer was used to seed the injectant with olive oil particles. The 3-dB frequency response of for this 0.5–1.0 μm diameter seed material has been previously established at 60–220 kHz (Ref. 19). The scattered light from both the red and green laser pulses was collected with the CCD camera described earlier. For the time-averaged Mie scattering images, only one laser was used, and the camera exposure was increased so that 30 laser pulses were captured on a single CCD image.

Shadowgraph

The optical system for the shadowgraph consisted of a mercury vapor light source and a mirror to form a parallel column of light. The beam was passed through the test section and onto a reflective screen to form the shadowgraph image. The shadowgraph images were digitized with the Kodak CCD camera already mentioned.

Five-Hole Probe

An Aeroprobe L-shaped, five-hole probe was used to measure the mean flow properties (pitot pressure and local Mach number). The probe had a blunted axisymmetric conical tip, with a 19-deg semivertex angle. The diameter at the base of the conical tip was 3.18 mm. The conical surface was instrumented with four elliptically shaped static pressure taps, which were formed from the 0.79-mm-diam holes that were drilled into the surface parallel to the cone axis. The four ports were located midway between the tip and base of the cone at 90-deg intervals around the circumference. The blunted tip housed a 0.79-mm pitot pressure port. The pitot pressure was monitored with a 0–0.69 MPa pressure transducer (Omega Model PX139-100A4V). The four static pressure ports were monitored with four 0–0.10 MPa pressure transducers (Model PX139-15A4V). The pitot and cone-static pressure transducer uncertainties were ±550 and ±330 Pa, respectively.

A semi-empirical calibration of the probe was performed. The calibration data spanned $M = 1.7$–5.5. Based on these data, a slight modification to the ideal calibration $[M_I = f_I(p_c/p_{t2})]$, which was based on normal shock and inviscid Taylor–MacColl conical flow theories (see Ref. 20) was developed and is given by $M = (1.23 - 0.061M_I) \cdot f_I(p_c/p_{t2})$. An uncertainty analysis accounting for transducer and position uncertainties was performed. Over the range of the calibration, the uncertainty in Mach number was fit, to within ±0.01, by the relation $\pm\Delta M \approx 0.016 \cdot [1.0 + (M - 1.7)^2]$. This relation shows that the uncertainty increased with Mach number squared. In the present experiments, the flow angles were not zero. However, when the average static pressure around the periphery of the cone is used, the probe is insensitive to flow angle for angles less than about 6.0 deg (Ref. 21); because of this 6.0-deg limitation, the five-hole probe data were restricted to the low-injection-pressure cases (first five cases listed in Table 2).

Five-hole probe contours were constructed at $x/d = 8.0$ by vertically traversing the probe in the y direction at 19 z locations across the span of the tunnel. The six center profiles had a spacing of $0.94d$, and the remaining outer profiles had a spacing of $1.88d$. A traverse system consisted of a 15W Bodine Electric Model NSH-12 dc fractional horsepower gear motor that drove a linear slide in the y direction. The axial and span locations were manually set. The traverse speed was set as 7.6 mm/s to ensure that probes had sufficient time to respond to the flow. The vertical position of the probe was recorded by an Omega Model LD100-150 linear voltage displacement transducer (LVDT). The uncertainty in the LVDT measurement was ±0.1 mm. The axial and span uncertainties were estimated as ±0.8 and ±0.4 mm, respectively.

All of the analog voltage signals were converted into digital signals with a Keithley low-gain, 12-bit data acquisition board (Model DAS-1802AO). The sampling frequency was set at 1.0 kHz. The profiles at each z location consisted of 80 points, where each point was an average 60 samples.

PSP

ISSI, Inc., Uni-FIB PSP was used. The paint contained two parts: an oxygen permeable flouroacrylic copolymer (FIB) binder and a fluorinated platinum porphyrin meso–tetra–pentaflourophenyl porphrine oxygen-sensitive probe molecule. The PSP was applied to the tunnel floor using an airbrush sprayer. The paint was cured at 65°C for 30 min to reduced the temperature sensitivity to 0.4%/°C. The paint was illuminated with two blue (464 nm) light

emitting diode (LED) light sources (0.25 W each). The luminescence output (650 nm) was acquired with a Pixelvision SpectraVideo 16-bit CCD camera (Model SV512V1A/PFT-95). Pressure tap data acquired during the tunnel run were used to build the PSP calibration. The paint calibration stemmed from the Stern–Volmer relationship (see Ref. 22), where the pressure was expressed as a function of I_{ref}/I. As suggested by the manufacturer, the calibration data were fit with a second-order polynomial; the standard deviation for the fit was within the ±330 Pa uncertainties of the port transducers. The overall uncertainty for the PSP, including wall calibration and temperature, was estimated as $\pm[(330)^2 + 0.0016 \cdot p^2]^{1/2}$ Pa.

Experimental Results and Discussion

Surface Oil Flow Visualization

Surface oil flow visualizations were acquired for all of the conditions listed in Table 2. The diamond injector results were divided into two basic categories: attached and detached leading-edge shocks. Representative examples of each diamond injector type are shown in Figs. 3a and 3b, where the freestream is from left to right, and the jet flow is directed outward from the paper. The high-pressure circular injector result is shown in Fig. 3c. When the attached case given in Fig. 3a (low pressure, $\alpha = 27.5$ deg) is examined, the first flow feature, moving from left to right, is a curved line of oil accumulation enclosing the diamond-shaped injector exit. This line is attached to the injector leading edge and is essentially collocated with the jet interaction shock in the region near the injector; this is confirmed with the PSP measurements to be described later. However, farther downstream, the shock wave strength decreased and approached a Mach wave, and hence, it was no longer coincident with the line of separation. The second curved line of oil accumulation that wrapped around the jet indicates the location of a small horseshoe vortex. Third, two wake vortex lines due to up-wash[10] were observed to emanate at the injector trailing edge. Fourth, between the wake vortex lines is the reattachment line. In general, the flow topologies for the detached shock cases, for example, Fig. 3b, were similar to those of the attached shock case. The obvious exceptions are 1) the detached leading-edge jet interaction shock and 2) the horseshoe vortex was more pronounced and reached farther upstream for the detached shock case. The circular injector flow topology (Fig. 3c) was very similar to the detached diamond injector (Fig. 3b). However, when compared to the detached diamond injector flow, the circular injector shock standoff distance was larger and the angle between the wake vortex lines was lower. In general, the described topology is very similar to the lower Mach number results of Tomioka et al.[16]

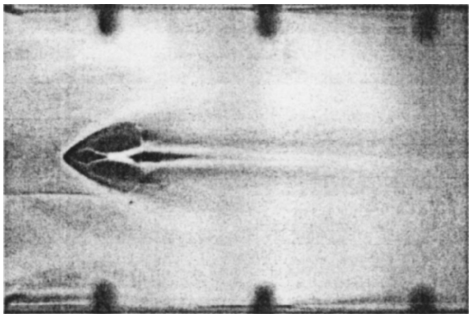

a) Low pressure, α = 27.5 deg

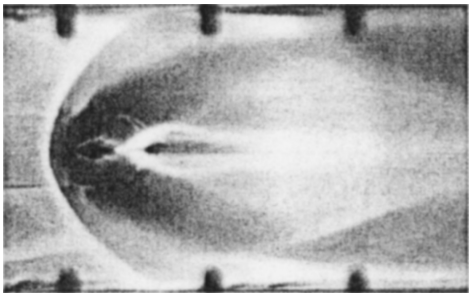

b) High pressure, α = 90 deg

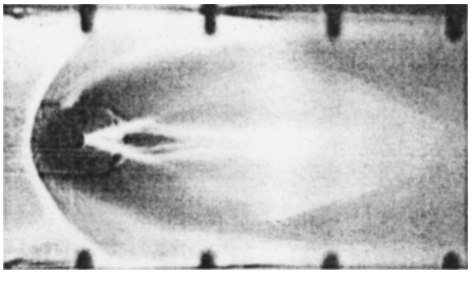

c) High pressure, α = 90 deg

Fig. 3 Representative surface oil flow visualizations.

On examination of the surface oil flow visualizations for all of the injection angles (10–90 deg) at both injection pressures, the following specific observations were drawn. First, the state of the leading-edge shock wave (attached or detached) for the diamond injectors depended on both α and the injector pressure. The attached shock (AS) cases are listed in Table 2. As indicated in Table 2, the shocks were attached for the low pressure, $\alpha = 10$ and 27.5 deg cases. The shock standoff distance was very small for the 45-deg case. As α increased from 10 to 45 deg, the leading-edge shock angle increased from 35 to 52 deg. The increase is explained by recognizing that the discharge coefficient, and hence mass flux, increased significantly with injector angle (Table 2). Moreover, as α increased, the three-dimensional relieving effect[20] decreased.

Focus now on the high-pressure results in Table 2. The shocks were attached for $\alpha = 10$ deg. For $\alpha = 10$–45 deg, the shock angles were nominally 10 deg larger than the corresponding low-pressure cases. Also, compared to the low-pressure data, the high-pressure wake regions were wider in the z direction, the wakes and wake vortices extended farther downstream, and the horseshoe vortices reached farther upstream. For the detached shock cases, the high-pressure shock strength was larger than the corresponding low-pressure results, as indicated by the larger lateral extent of the nearly normal shock region and the larger shock wave detachment distance. The explanation for all of these observations is that the higher pressure jets expanded more when injected into the freestream, creating additional blockage and penetration, and, thus, the preceding listed observations.

Shadowgraph Photography

Shadowgraph images were acquired for all of the conditions listed in Table 2. Representative examples of the three categories listed earlier are shown in Fig. 4. In Figs. 4, the crossflow is from left to right, and the injector port is in the tunnel floor. The attached shock case (Fig. 4a) corresponds to the low-pressure, $\alpha = 27.5$ deg test condition. A clearly defined jet interaction shock is depicted, and the barrel shocks are faintly visible. The high-pressure, $\alpha = 90$ deg case is shown in Fig. 4b. The main difference between the detached and attached shock shadowgraphs is the presence of the lambda shock, which was created by the stronger detached bow shock wave interaction with the tunnel boundary layer. The shock structure for the circular injector (Fig. 4c) was similar to that for the detached injector.

Examination of all of the shadowgraphs confirmed the trends described in the preceding section and listed in Table 2. Specifically for the low-pressure, $\alpha = 10$ and 27.5 deg cases, leading-edge lambda shocks were not present, indicating an absence of upstream flow separation. For $\alpha = 10$–45 deg, the shock angles increased from 30 to 49 deg with jet incidence angle, demonstrating that the shock strength, and hence, total pressure loss, increased with jet incidence angle. Quantification of the shock losses is described in the "Approximate Shock Loss Analysis" section. The 90-deg diamond and 90-deg circular cases both had lambda shocks, which indicated flow separation. Barrel shocks were visible for the 45–90 deg cases. However, they were not visible for the remaining two lower angle cases. It was expected that, for the lower angles, the barrel shocks were not as strong due to the lower discharge coefficients and subsequent reduced pressure (listed in Table 2). In addition, the jets did not penetrate very far into the freestream; hence, the barrel shocks were

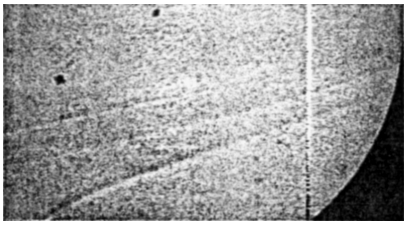

a) Low pressure, α = 27.5 deg

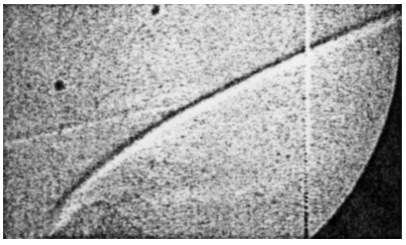

b) High pressure, α = 90 deg

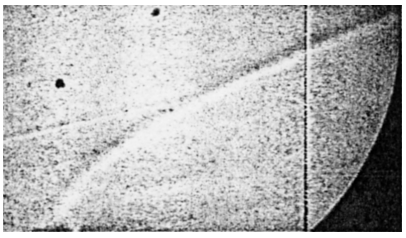

c) High pressure, α = 90 deg

Fig. 4 Representative shadowgraph images.

blurred by the tunnel boundary layer. The initial shock angles for each incidence angle were noticeably larger (8–13 deg) for the high-pressure conditions as compared to the corresponding low-pressure cases. Lambda shocks were present for all but the lowest angle case, and the barrel shocks were clearly visible in all of the high-pressure shadowgraphs.

Mie Scattering Imagery

Examples of instantaneous and time-averaged Mie scattering flow visualizations are presented in Fig. 5. The instantaneous images for the low-pressure, $\alpha = 27.5$ and 90 deg cases are compared in Figs. 5a and 5b. In both images, the freestream flow is from left to right. The instantaneous image shows that large-scale turbulent structures were present in the jet plumes; however, the size of the structures near the jet orifice appeared to have increased with increasing incidence. For the 90-deg case shown in Fig. 5b, the tunnel was intentionally run approximately 5.0 K below the oxygen liquefaction temperature to produce Rayleigh scattering from the condensed liquid oxygen in the freestream. Hence, the tunnel boundary layer, just upstream of the injector port, and the jet interaction shock were visible due to vaporization of the oxygen in the warmer boundary layer and across the shock. This rather unique flow visualization indicated that even though the jet interaction shock for this case was detached near the wall (Table 2), it reattached to the jet near the point where the plume bent over toward the freestream direction. In addition, the jet plume narrowed in this region, which is indicative of the plume spreading more in the lateral direction.[13] Figure 5a shows a similar phenomenon.

The time-averaged data (examples in Figs. 5c–5e) show the upper edge more clearly and, hence, the mean penetration of the plume into the freestream. Time-averaged Mie scattering images were obtained for all of the cases listed in Table 2. It was also apparent that the plume narrowing described in the earlier was present for all of the diamond injectors and absent for the circular injector. Visual measurements of the centerline penetration (y_p/d) were obtained from these data for x/d less than about 8.0. The jagged plume edges seen in Fig. 5 resulted in scatter in the y_p/d measurements ranging

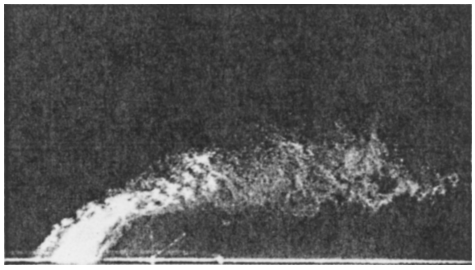

a) Upper: low pressure, α = 45 deg

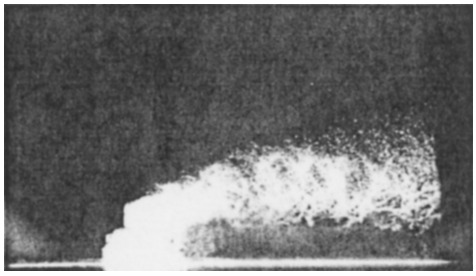

b) Lower: low pressure, α = 90 deg

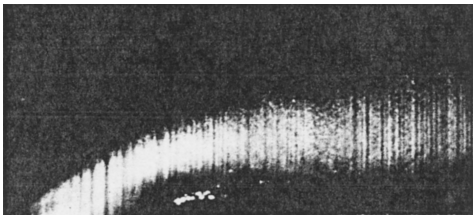

c) Low pressure, α = 27.5 deg

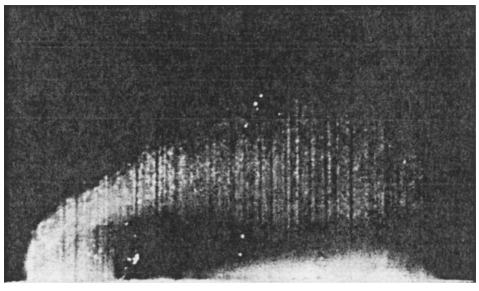

d) High pressure, α = 90 deg

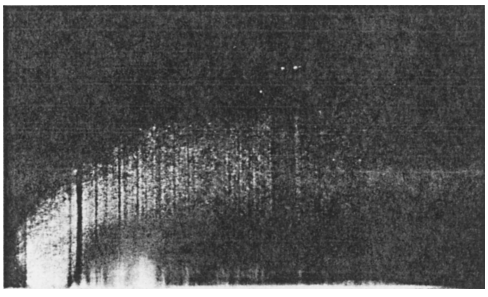

e) High pressure, α = 90 deg

Fig. 5 Representative Mie scattering flow visualizations.

from about ± 0.1, close to the jet exits, to approximately ± 0.2 at the downstream limit of the measurement ($x/d \approx 8.0$).

Various power-law correlation methods have been proposed for penetration.[8,13] A generalized form for these correlations for the present sonic injection into a Mach 5.0 freestream was written as $y_p/d = f_p\ (\xi)$, where $\xi = J_{\text{eff}}^m (x/d)^n$. For the present study, $J_{\text{eff}} = J \sin\alpha$, and the values of J are listed in Table 2. Figure 6 shows all of the penetration data with the scaling just given. As indicated in Fig. 6, the diamond and circular injector data collapse reasonably well (variation in y_p/d is within the scatter of the data)

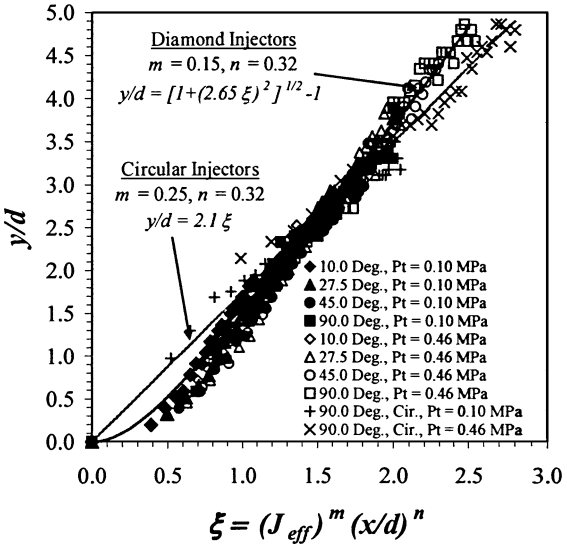

Fig. 6 Penetration correlation results.

onto to two separate curves, one for the diamond injectors and the other for the circular injectors. For both data sets, n was found to be nominally 0.33; this value is consistent with previous studies at lower supersonic freestream Mach numbers.[13] Values of 0.15 and 0.26 for m were found to collapse the diamond and circular port data, respectively. The function $f_p(\xi)$ for the circular injector data was the straight line $y_p/d = 1.93\xi + 0.40$, where the linear form agrees with previous studies.[13] The nonzero intercept reflects that the plume expanded upstream of the injector port (Fig. 5d). For the diamond injector, $f_p(\xi)$ was linear to within the experimental scatter for ξ greater than about 1.0, with a slope of 2.65. However, for ξ less than 1.0, the data systematically dipped below the linear trend. A hyperbolic curve was incorporated to fit the data over the full range of ξ shown in Fig. 6; the resulting equation was $y_p/d = [1 + (2.65\xi)^2]^{1/2} - 1$. The reproduction of the penetration was within the expected uncertainty of the data.

Penetration measurements at $x/d = 7.5$ are listed in Table 2 (eight column) for all of the test conditions. From these data, the following specific conclusions were drawn. First, for the diamond injectors, the penetration at $x/d = 7.5$ increased by 70 and 90% as α increased from 10 to 90 deg, for the low- and high-pressure cases, respectively. Second, for given incidence, the penetration increased by nominally 30% going from low to high pressure for all of the diamond injectors; for the circular injector, the increase was 50%. Also, comparing the 90-deg diamond and circular injectors, the magnitude of the penetration was essentially the same at $x/d = 7.5$. The data and correlations shown in Fig. 6 also show that the penetration for the circular injectors at both pressures exceeded that of the 90-deg diamond injectors, for $x/d < 7.5$. However, the plume trajectories, that is, slopes, for the 90-deg diamond injectors were approximately 30% larger than those for the circular port at $x/d = 7.5$. Hence, it is anticipated that the downstream penetration for the 90-deg diamond injectors would exceed that of the circular injectors, which agrees with a previous study.[16]

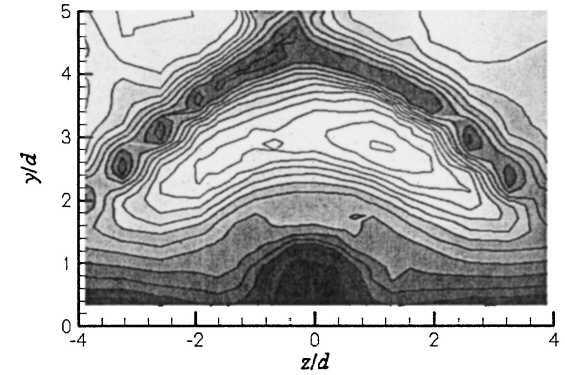

a) α = 45 deg

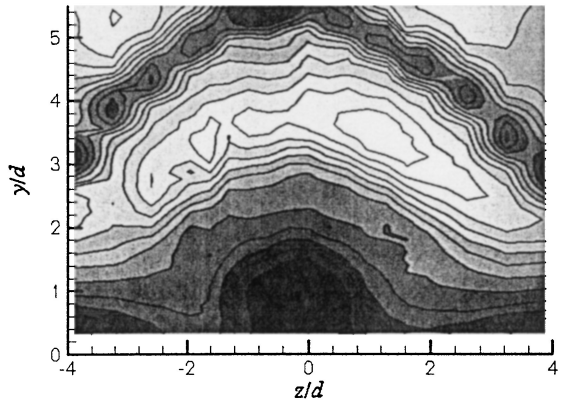

b) α = 90 deg

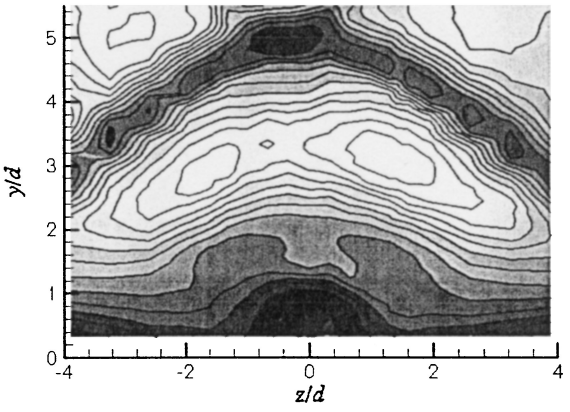

c) α = 90 deg, circular

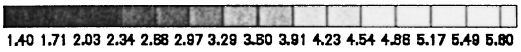

Fig. 7 Mach number contours (low pressure, x/d = 8.0).

Mach Number Contour Data

Representative Mach number contours are shown in Fig. 7. The Mach number contour for the low-pressure, $\alpha = 45$ deg diamond-shaped injector (Fig. 7a) is examined first. From at the top, the interaction shock wave is the roughly diamond-shaped structure with the vertex located at $z/d \approx 0.0$, $y/d \approx 4.2$ and that arched down to $z/d \approx \pm 3.9$ at $y/d \approx 2.0$. The narrow high Mach region below the shock is the inviscid shock layer between the shock and the plume. The lower extent of the shock layer corresponds to the upper boundary of the plume, which at the centerline ($z/d = 0.0$) was located at $y/d \approx 2.8$–3.2 (Fig. 6). At the bottom of the contour, the wake or up-wash[10] region is seen as the low Mach, semicircular region centered at $z/d = 0.0$. The vertical extent of this region ($y/d \approx 1.4$) coincides with lower edge of the plume as inferred from Fig. 5b. The tunnel boundary layers are also noticeable on both sides of the contour. The boundary layer thinning in the areas adjacent to the wake resulted from entrainment of low-momentum boundary-layer fluid into the plume and wake.[11] The plume is above the wake region. Although the plume edges are not discernable in Fig. 7a, the expected kidney bean[6] shape of the plume can be inferred from the Mach contours. Specifically, from the midpoint of the lower edge of the plume ($z/d = 0.0$, $y/d \approx 1.4$), and traversing around the plume in a counterclockwise direction, the plume boundary is expected to have wrapped down and around the wake region, dipping closer to the wall in the region where the boundary layer thinned, $z/d \approx 1.0$, (Ref. 11). Although, the exact lateral extent of the plume is not discernible,

the dog-ear structure located near $z/d \approx 1.0$, $y/d \approx 1.5$ is indicative of the low-momentum boundary-layer fluid induction into the right vortex associated with the counter-rotating vortex pair.[10,11] Symmetry about the z axis, to within experimental uncertainty, was observed.

The Mach number contour for the detached diamond injector is presented in Fig. 7b. The overall interpretation of Fig. 7b is similar to that for Fig. 7a. The notable differences are 1) the interaction shock extended about 25% farther into the freestream; 2) the shock shape had more curvature, which is consistent with a detached bow shock; and 3) the low Mach upwash region was significantly larger, indicative of the increased mass flow rate and penetration (Table 2).

The Mach number contour for the circular injector is given in Figs. 7c. The flow features in Fig. 7c are very similar to Fig. 7b. However, the penetration of the interaction shock was approximately 10% lower than that for the case in Fig. 7b. The circular injector low Mach upwash region was significantly smaller than that for the diamond injector in Fig. 7b. However, the dog-ear structures at $z/d \approx \pm 1.0$, $y/d \approx 1.5$ are more pronounced than for either Fig. 7a or Fig. 7b, which indicates stronger plume vorticity.

PSP

PSP data were acquired for all of the conditions listed in Table 2. Representative surface pressure contours, for the same three conditions shown in Figs. 3–5, are shown in Fig. 8. The pressure distributions reflect the flow topologies described with respect to Fig. 3. The pressure contour for the low-pressure, 45-deg injector is presented in Fig. 8a. The pressure ratio (p/p_∞) increased to approximately 2.3 across the interaction shock. The surface pressure subsequently decreased through an expansion as the flow wrapped around the injected fluid to a relatively low wake pressure, $p/p_\infty \approx 0.3$; this low pressure was expected.[8] The high-pressure, 90-deg injector surface pressure distribution is given in Fig. 8b. For this case, the shock wave was detached. The horseshow vortex, the high-pressure structure that wrapped around the injector, was a dominant high-pressure flow structure. The peak pressure ratio within the horseshoe vortex was approximately 4.2. The pressure ratio in the wake, just downstream of the injection port was nominally 0.3. The surface pressure field for the circular injector (Fig. 8c) contained the same structures as the diamond injector (Fig. 8b). However, the shock standoff distance was significantly larger (123%) than for the corresponding diamond flow in Fig. 8b. The peak pressure ratio for the high-pressure circular injector was 4.9; the minimum pressure ratio in the wake was 0.15. The effective backpressure was measured from the surface pressure plots as the average pressure around the periphery (within approximately $0.2d$ of the injector edges) of the injector; the resulting ratios λ from this analysis are listed in Table 2.

For perpendicular injection through circular orifices, the initial jet penetration has been shown to be strongly dependent on the p_j/p_{eb} (Ref. 23). Hence, that pressure ratio was also computed and included in Table 2. As indicated, for each of the two constant total pressure data sets, p_j/p_{eb} decreased by 25–30% as α increased from 10 to 90 deg. It is expected[23] that this decrease worked to decrease the initial penetration and, thus, counteracted a portion of the penetration increase that would have resulted from the increase in J_{eff} that resulted from the increase in incidence angle.

Centerline pressure traces for all of the cases in Table 2 were obtained from the PSP measurements and are plotted in Fig. 9. The leading edge of the injector was at $x/d = 0.0$. The trailing edge of the diamond and circular injectors were at $x/d = 2.4$ and 1.0, respectively. The peak pressure just upstream of the injector for the detached cases and a given geometry increased with increasing injector pressure. For a given pressure ratio, the 90-deg circular injectors produced larger peak pressures than did the 90-deg diamond injector, which indicated stronger shocks for the circular injectors. Standoff distances for the detached shock waves as estimated from this Fig. 9 are summarized in Table 2. The standoff distance increased with both injector pressure and incidence angle and was largest for the circular injector. The wake pressure traces, from just downstream of the injector ports to $x/d \approx 3.5$, for all but the low-pressure 10-deg diamond injector, were similar in magnitude and shape. The low-pressure, 10-deg diamond injector had a very low discharge coefficient, and hence, the overall flow disturbances were small. The gap in the data between $x/d = 3.5$ and 5.0 was the result of a imperfection in the paint coverage due to the sealing of a port in the floor; this port is clearly visible in the contours shown in

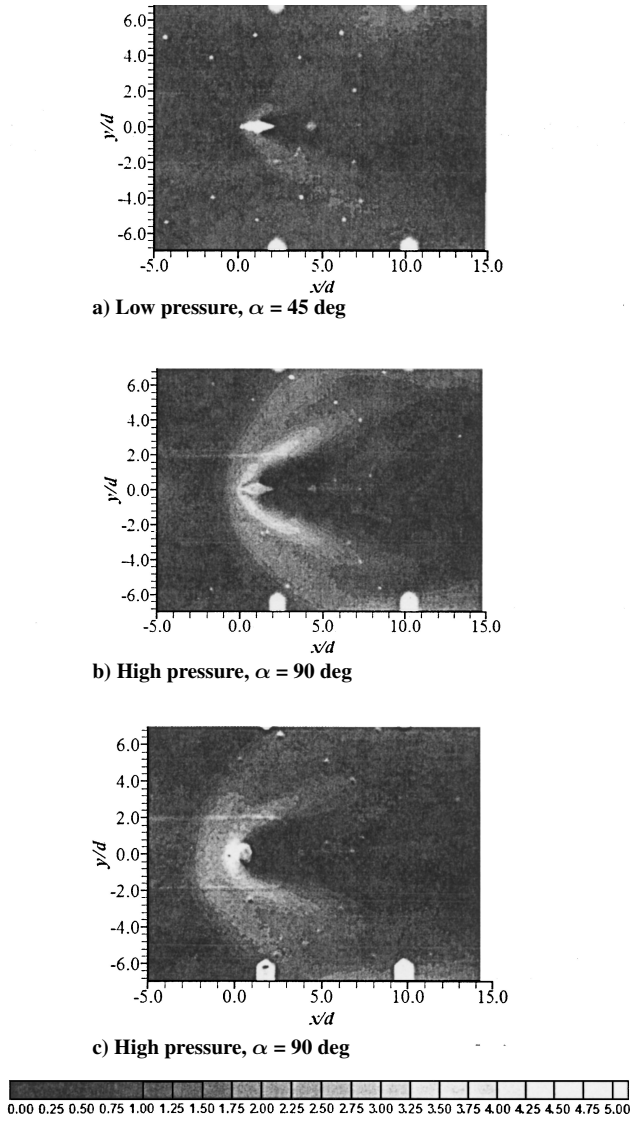

a) Low pressure, α = 45 deg

b) High pressure, α = 90 deg

c) High pressure, α = 90 deg

Fig. 8 Representative PSP results, p/p_∞.

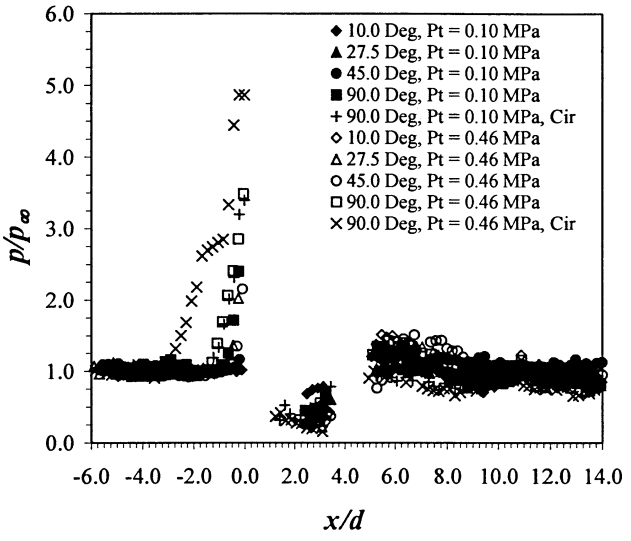

Fig. 9 Centerline pressure traces.

Fig. 8. Downstream of this region, the flow was compressed and subsequently relaxed back to nearly the freestream pressure.

Approximate Shock Loss Analysis

To estimate the bow shock total pressure loss, the three-dimensional interaction shock shape was modeled from the surface shock shape, the centerplane shock shape, and cross-sectional shock shape. The cross-sectional shock shape was estimated from the five-hole probe, low-pressure Mach number data at $x/d = 8.0$. The cross-sectional jet interaction shock shapes, nondimensionalized by the maximum y, z coordinates, at $x/d = 8.0$, were fit with the following third-order polynomial $y/y_{\max} = a(z/z_{\max})^3 + b(z/z_{\max})^2 + c(z/z_{\max}) + d$, where the coefficients a–d were found by applying boundary conditions at $z/z_{\max} = 0$ and $z/z_{\max} = 1$. The best agreement to the data was achieved with the following boundary conditions: at $z/z_{\max} = 0$, $y/y_{\max} = 1$ and $\mathrm{d}(y/y_{\max})/\mathrm{d}(z/z_{\max}) = -0.4$ and at $z/z_{\max} = 1$, $y/y_{\max} = 0$ and $\mathrm{d}(y/y_{\max})/\mathrm{d}(z/z_{\max}) = -0.3$. The mean square errors for all cases varied from 4.0 to 7.0%. The shock shape along the tunnel surface, that is, $z_{\max}(x/d)$, was evaluated from the data in Figs. 3 and 8. The centerline shock shape, that is, $y_{\max}(x/d)$, was directly measured from the shadowgraph photographs (Fig. 4). With the three-dimensional shock shape modeled, the unit normal vector $\hat{\boldsymbol{n}}$ to the shock surface was calculated by computing the gradient to the shock shape function. With the unit normal, the normal component of the Mach number over the shock surface was found by the relation $M_n = M_1 \hat{i} \cdot \hat{\boldsymbol{n}}$. Because the jet was introduced into the tunnel boundary layer, M_1 was evaluated as a function y/d using the Van Driest II compressible turbulent velocity profile scaling (see Ref. 24). The shock total pressure was then estimated with the normal component of the Mach number using normal shock theory.[20] The resulting area averaged total pressure losses, that is,

$$\Pi = \iint_S \frac{p_{t2}}{p_{t1}}\,\mathrm{d}s \Big/ \iint_S \mathrm{d}s$$

were computed for $x/d \leq 8$, where S is the shock surface area, and the integrand in the numerator is a function of M_n for air. The results are listed in Table 2. For the high-pressure cases, the normalized shock cross section fit was assumed. To quantify the scatter due to the curve fit, the shock loss was also calculated for the 45-deg case using two additional curves that defined upper and lower bounds in the experimental data for the scaled cross-sectional shock fit. The resulting uncertainty was approximately ±4.0%. The shock loss data in Table 2 demonstrate that losses decreased with decreasing jet incidence angle and injection pressure. The largest pressure losses were incurred by the 90-deg, circular injector.

Conclusions

An experimental study to characterize the near-field ($x/d < 8.0$) flow for gaseous injection through diamond shaped orifices (15-deg half-angle) at four incidence angles, 10, 27.5, 45, and 90 deg, and two total pressures, $P_{tj} = 0.10$ and 0.46 MPa, into a high Reynolds number $Re/\mathrm{m} = 53 \times 10^6$, Mach 5.0 freestream was performed. A 90-deg circular injector, with the same exit port area and total pressures, was examined for comparative purposes. The experimental methods included surface oil flow visualization, shadowgraph photography, Mie scattering flow visualization, PSP and a pitot–cone five-hole pressure probe. Flowfield documentation, jet penetration, and shock-induced total pressure loss were derived from these data. From these data, the following specific conclusions were drawn. First, near-wall attachment of the jet interaction shock wave depended on both incidence angle and injector pressure, where the shock remained attached at higher incidence angles at the lower injection pressure. Second, $\delta/d = 1.6$; hence, the detached shocks separated the incoming boundary layer and generated the familiar lambda shock structure. Lambda shocks were not observed for the attached shock cases. Third, near-field, $x/d < 8.0$, centerline penetration correlations $y_p/d = f_p(\xi)$, where $\xi = J_{\mathrm{eff}}^m (x/d)^n$, were developed for both the diamond and circular injectors; f_p was hyperbolic and linear for the diamond and circular injectors, respectively. Fourth, for the detached cases, the highest surface pressures were associated with the horseshoe vortex. Fifth, the upstream peak pressures for the detached cases, for a given injector geometry, increased with increasing injector pressure. Sixth, for a given pressure ratio, the 90-deg circular injectors produced largest peak pressures. Seventh, the shock-induced total pressure losses decreased with decreasing jet incidence angle and injection pressure, where the largest losses were incurred by the 90-deg, circular injector.

Acknowledgments

The authors thank S. Walker and J. Schmisseur from the Air Force Office of Scientific Research for sponsoring this research.

References

[1]Beach, H., and Blankson, I., Jr., "Prospects for Future Hypersonic Air-Breathing Vehicles," AIAA-91-5009, Dec. 1991.

[2]Freeman, D. C., Jr., Reubush, D. E., McClinton, C. R., Rausch, V. L., and Crawford, J. F., "The NASA Hyper-X Program," *48th International Astronautical Congress*, NASA-97-48IAC-DCF, Turin, Italy, Oct. 1997.

[3]Heiser, W., and Pratt, D., *Hypersonic Airbreathing Propulsion*, AIAA Education Series, AIAA, Washington DC, 1994, pp. 277–378.

[4]Weber, R., and McKay, J., "Analysis of Ramjet Engines Using Supersonic Combustion," NACA TN-4386, Sept. 1958.

[5]Riggins, D., McClinton, C., Rogers, R., and Bittner, R., "Investigation of Scramjet Injection Strategies for High Mach Number Flows," *Journal of Propulsion and Power*, Vol. 11, No. 3, 1995, pp. 409–418.

[6]Schetz, J., Thomas, R., and Billig, F., "Mixing of Transverse Jets and Wall Jets Supersonic Flow," *Separated Flows and Jets*, edited by V. Kozlov and A Dovgal, Springer-Verlag, Berlin, 1991, pp. 807–835.

[7]Wilson, M., Bowersox, R., and Glawe, D., "An Experimental Investigation of the Role of Downstream Ramps on a Supersonic Injection Plume," *Journal of Propulsion and Power*, Vol. 15, No. 3, 1998, pp. 432–439.

[8]Zukowski, E., and Spaid, F., "Secondary Injection of Gases into a Supersonic Flow," *AIAA Journal*, Vol. 2, No. 10, 1964, pp. 1697–1705.

[9]Schetz, J., and Billig, F., "Penetration of Gaseous Jets Injected into a Supersonic Stream," *Journal of Spacecraft and Rockets*, Vol. 3, No. 11, 1966, pp. 1658–1665.

[10]Chenault, L., Beran, P., and Bowersox, R., "Second-Order Reynolds Stress Turbulence Modeling of Three-Dimensional Oblique Supersonic Injection," *AIAA Journal*, Vol. 37, No. 10, 1999, pp. 1257–1269.

[11]McCann, G., and Bowersox, R., "Experimental Investigation of Supersonic Gaseous Injection into a Supersonic Freestream," *AIAA Journal*, Vol. 34, No. 2, 1996, pp. 317–323.

[12]McClinton, C., "The Effects of Injection Angle on the Interaction Between Sonic Secondary Jets and a Supersonic Freestream," NASA TN D-6669, Feb. 1972.

[13]Gruber, M., Nejad, A., Chen, T., and Dutton, C., "Mixing and Penetration Studies of Sonic Jets in a Mach 2 Freestream," *Journal of Propulsion and Power*, Vol. 11, No. 2, 1995, pp. 315–323.

[14]Barber, M., Schetz, J., and Roe, L., "Normal Sonic Helium Injection Through a Wedge-Shaped Orifice into a Supersoni Flow," *Journal of Propulsion and Power*, Vol. 13, No. 2, 1997, pp. 257–263.

[15]Fan, H., and Bowersox, R., "Gaseous Injection through Diamond Orifices at Various Incidence Angles into a Hypersonic Freestream," AIAA Paper 2001-1050, Jan. 2001.

[16]Tomioka, S., Jacobsen, L., and Schetz, J., "Sonic Injection from Diamond-Shaped Orifices into a Supersonic Crossflow," *Journal of Propulsion and Power*, Vol. 19, No. 1, 2003, pp. 104–114.

[17]Deissler, R., "Analysis of Turbulent Heat Transfer and Flow in the Entrance Region of Smooth Passages," NACA TN 3016, Oct. 1953.

[18]Shames, I., *Mechanics of Fluids*, 4th ed., McGraw–Hill, New York, 2003, pp. 435, 436.

[19]Bowersox, R., "Combined Laser Doppler Velocimetry and Cross-Wire Anemometry Analysis for Supersonic Turbulent Flow," *AIAA Journal*, Vol. 34, No. 11, 1996, pp. 2269–2275.

[20]Anderson, J., *Modern Compressible Flow*, 2nd ed., McGraw–Hill, New York, 1990, pp. 294–306.

[21]Volluz, R., *Handbook of Supersonic Aerodynamics, Section 20, Wind Tunnel Instrumentation and Operation*, Vol. 6, Ordnance Aerophysics Lab., NAVORD Rept. 1488, Daingerfield, TX, Jan. 1961.

[22]Davis, J., Goss, L., Crafton, J., and Dale, G., "Performance Characteristics and Methods of Application of Pressure Sensitive Paints," 8th Annual Pressure Sensitive Paint Workshop, NASA Langley Research Center, Langley, VA, Oct. 2000.

[23]Billig, F., Orth, R., and Lasky, M., "A Unified Analysis of Gaseous Jet Penetration," *AIAA Journal*, Vol. 9, No. 6, 1971, pp. 1048–1058.

[24]White, F., *Viscous Fluid Flow*, 2nd ed., McGraw–Hill, New York, 1991, pp. 543–556.